CrossMark

Microwave synthesis of hydroxyapatite bioceramic and tribological studies of its composites with $SrCO_3$ and ZrO_2

C. R. Gautam[1] · M. Tamuk[3] · C. W. Manpoong[3] · S. S. Gautam[3] · Sunil Kumar[2] · Anod Kumar Singh[2] · V. K. Mishra[4]

Abstract Hydroxyapatite (HAp) powders were prepared successfully using microwave-assisted co-precipitation method. HAp powder was characterized by X-ray diffraction (XRD), fourier transform infrared spectroscopy (FT-IR) and Raman spectroscopy for structural confirmation of the prepared material. Further, six composites of HAp with $SrCO_3$ and ZrO_2 were synthesized to study the morphological and tribological behaviour. Three composites of HAp with three varying 2, 4, 6 wt% of $SrCO_3$ and similarly other three with ZrO_2 were prepared using solid-state route method. Scanning electron microscopy (SEM) analysis confirmed that the presence of $SrCO_3$ and ZrO_2 among HAp particles helps in grain growth during the sintering processes. The tribological study reveal that the inclusion of $SrCO_3$ and ZrO_2 in pure HAp enhanced the resistance to wear and specific wear rate. The average grain size of HAp–ZrO_2 was observed more in comparision to the average grain size of the HAp–$SrCO_3$. The values of the specific wear rate and wear of HAp–$SrCO_3$ and HAp–ZrO_2 composite ceramics lies in the range from $4.13{,}239 \times 10^{-5}$ to 5.44517×10^{-5} mm^3/Nm and 4.68693×10^{-5} to 6.10099×10^{-5} mm^3/Nm, respectively.

Introduction

The properties of advanced ceramics have made them important for much extraordinary applications. Bioceramics lie in the class of that advanced ceramic materials. The kind of ceramics having biological applications such as artificial hip, knee, teeth and other prosthesis is termed as bioceramics [1, 2]. The porous HAp bioceramics are more useful due to the promotion of the bone tissues along with enough strength [3]. The bioceramics used in hip/knee/femur replacements are designed to be so porous that it stimulates natural bone growth as well as tissue formation around the artificial joint surfaces with suitable toughness [4]. Bioceramics are being used for the repair and reconstruction of skeletal diseases and disorders because of their specific positive response when used as an implant and dental applications [5]. The most important difference between bioceramics and the other implanted materials is that bioceramics involve in the metabolic processes of the organism. They have the ability to be adapted in surface or to the bio-medium with excellent in vivo response without any inflammatory problem [6]. In this view it is useful to dwell on the biological properties of bioactive ceramic implants, particularly those of calcium phosphate, which can be controlled to be completely reabsorbed in the desired course of time [7]. Most of the bioceramics are particularly calcium phosphate-based materials.

Hydroxyapatite (HAp): $Ca_{10}(PO_4)_6(OH)_2$ is chemically similar to the inorganic part of human bone and teeth materials [8, 9]. It is much useful when bioactive calciumphosphat ceramics have excellent biocompatibility with

✉ C. R. Gautam
gautam_ceramic@yahoo.com

1 Department of Materials Science and Nanoengineering, Rice University, Houston, TX, USA

2 Advanced Glass and Glass Ceramic Research Laboratory, Department of Physics, University of Lucknow, Lucknow 226007, UP, India

3 Department of Mechanical Engineering, North Eastern Regional Institute of Science and Technology, Itanagar 791109, Arunachal Pradesh, India

4 Department of Physics, Banaras Hindu University, Varanasi 221005, India

natural hard as well as soft tissues [10]. HAp has momentous applications mainly as bone graft/substitute material (as a coating material on metal implant) or scaffolds due to its good biocompatibility, better bone and tissue bonding ability, compositional similarity with the inorganic components of human bone and teeth. In spite of being an excellent biomaterial having tens of merits the pure form of HAp cannot be used as bone substitute due to its poor mechanical strength, although, possessing excellent chemical resistance, compressive strength and wear resistance [11]. Therefore, the improvement in the mechanical strength of HAp is quite necessary hence, it has been the burning interest of scientists. Since the bone is the natural composite with enormous strength, the human femur has the capability to bear the load of 1650 kg which has not been considered so far. But from above, we can be sure that different composites of HAp may have better strength and other mechanical properties. HAp composites have several advantages such as improved fracture strength and toughness with improved machinability [12]. The earlier studies on HAp-based composites showed a little bit enhancement in their mechanical behaviour [13]. In terms of mechanical and tribological properties, nanocomposite of 10 wt% of dopant in HAp-based bone cement exhibits optimum performance as compared to others and these results play a vital role in the field of orthopaedic [14]. Another HAp composite with boron nitrate can offer excellent mechanical properties showing significant improvement in the wear resistance [15]. This admirable enhancement in wear resistance may be due to the lattice mismatch between HAp and boron nitrate leads which offers the coherent bonding and consequently the strong interface. A HAp composite with scratch using single-phase high crystalline nano HAp with bovine bone composition shows appropriate improvement in mechanical and tribological properties [16]. Different nanostructures of HAp also affect the mechanical properties of the composite. Thus the tribological and other properties of these composite can be greatly modified using different sized particles [17]. As we know that the moving from micro-to-nano scale, the surface-to-volume ratio increases which provides more substrate surface for cell adhesion and shows better mechanical properties. The mechanical properties can be greatly tailored by changing the HAp powder morphology [18]. Therefore, the nanotechnology can also help us in the task to improve the mechanical properties of HAp-based composites. Incorporation of additive/dopant creates disorders and defects in HAp crystal lattice to foster the mechanical properties [19–21]. There are a number of techniques viz. hydrolysis [22], sol–gel [23], hydrothermal [24] and microwave irradiation techniques [25, 26] to prepare the HAp NPs. Microwave irradiation technique is an extremely advantageous

technique over others. It is energy saving, time saving and eco-friendly too [25, 26]. Morphology of HAp calcium phosphate is strongly dependent on physico-chemical conditions such as stoichiometry, pH, rate of addition, ionic strength, temperature etc. of the synthesis process, so these parameters should be precisely controlled. HAp is the most stable form of calcium phosphate at normal temperature, in the pH range from 4–12 with Ca/P molar ratio being 1.67 for maintaining its stiochiometry [25–27].

By considering the literature, we plan to synthesize the HAp nanoparticles (NPs) and its different composites with different wt% of strontium carbonate ($SrCO_3$) and zirconia (ZrO_2) which are biologically acceptable materials [28–30]. The 0, 2, 4 and 6 wt% of strontium carbonate and zirconia are supposed to be added into a nanosized morphology of HAp powder. In the present study, we report the comparative study of tribological characteristics of two different composites of HAp with $SrCO_3$ and ZrO_2. In order to see the effect of additives ($SrCO_3$ and ZrO_2) on the growth mechanism of HAp NPs, the structural characterizations were also carried out. Either the present composite biomaterials have enough mechanical strength comparative to natural mammalian bone or this study will also be extremely helpful in the further development of bone replacement composite ceramics.

Experimental procedure

Materials and synthesis of nano hydroxyapatite powder

A simple co-precipitation method was used to prepare nano-sized hydroxyapatite HAp powder. In the microwave-assisted synthesis of HAp, calcium nitrate tetrahydrate ($Ca(NO_3)_2 \cdot 4H_2O$) as source of calcium, disodium hydrogen phosphate (Na_2HPO_4) as source of phosphorous and ethylene diamine tetra acetic acid (EDTA) as capping reagent have been taken. All the reagents were purchased from Merck Chemise having purity > 99 % and were used without any further purification. The molar ratio of ($Ca(NO_3)_2 \cdot 4H_2O + SrCO_3/ZrO_2$): EDTA:$Na_2HPO_4$ was maintained as 5:5:3. The calculated weight amount of calcium nitrate was introduced into 50 ml of double distilled water for complete dissolution, there after 50 ml solution of Na_2HPO_4 was poured into it. The nominal compositions of HAp powder has been listed in Table 1. The pH values of the solutions were adjusted up to 13 by adding suitable number of NaOH pellets and was stirred up to 45 min. The obtained aqueous solution was kept for 30 min into a microwave refluxing oven system with 750 W radiation power. The microwave oven along with refluxing system is shown in Fig. 1. The samples have been

Table 1 Nominal compositions of HAp powder

Chemicals	Mol. wt. (g/mol)	Molarity (mol.)	Purity (%)	Amount of chemicals $\frac{100}{Purity} \cdot \frac{(MxMol.wt.)100}{1000}$
EDTA	292.24	0.1	98	2.98204
$Ca(NO_3)_2 \cdot 4H_2O$	236.15	0.1	98	2.40969
Na_2HPO_4	141.36	0.06	98	0.86569
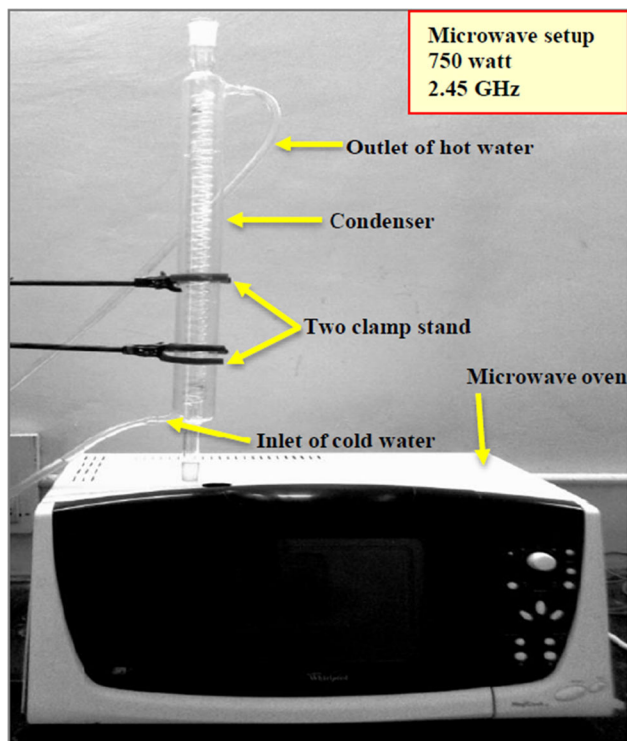
Fig. 1 Household microwave setup with refluxing system employed in present synthesis

Fig. 2 Methodology flowchart for the synthesis of HAp

synthesized using exposing reagents for 30 min in alternative steps of 5 s and 10 s in on and off conditions, respectively. Partially settled milky suspension was allowed to cool at room temperature inside the microwave oven. The precipitate was washed triply with double distilled water and was dried in a hot air oven at 150 °C for 4 h. The powder thus obtained was HAp calcium phosphate and grind into more fine powder. In order to obtain the HAp powder of high purity and crystallinity, sodium by-product was eliminated from the powder during calcination. Thus, the powder was further heat treated by its calcination at 800 °C for 3 h of holding time to form well-crystalline HAp powder. The obtained powders were then characterized using various techniques like XRD, FT-IR, Raman analysis to confirm its formation and achieve its composites with $SrCO_3$ and ZrO_2. The methodology flowchart for the entire synthesis of the material is shown
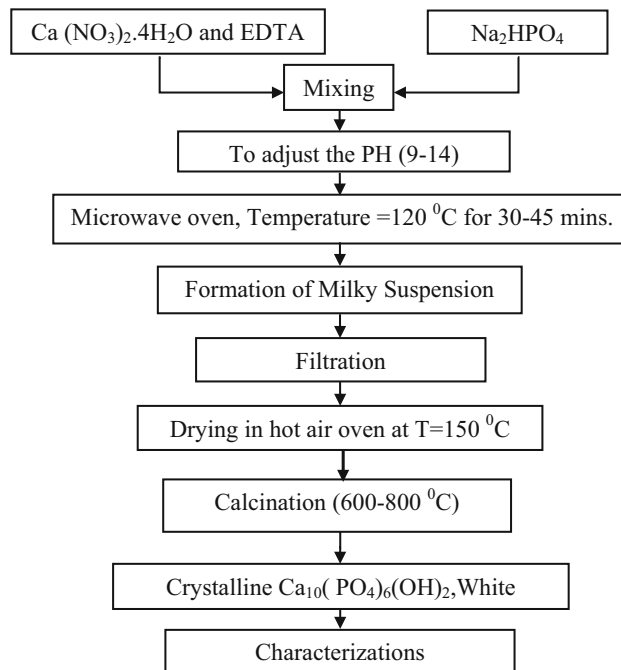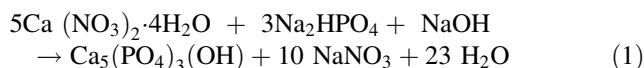
in Fig. 2. The chemical reaction for synthesis of HAp may be given as below in Eq. (1):

$$5Ca(NO_3)_2 \cdot 4H_2O + 3Na_2HPO_4 + NaOH$$
$$\rightarrow Ca_5(PO_4)_3(OH) + 10\ NaNO_3 + 23\ H_2O \qquad (1)$$

Six composites of HAp with $SrCO_3$ and ZrO_2 were formed to investigate the tribological characteristics and comprehensive analysis. Three composites of HAp with three varying 2, 4, 6 wt% of $SrCO_3$ and similarly other three with ZrO_2 were prepared. These composites were made by grinding the particular wt% of $SrCO_3/ZrO_2$ with pure HAp for at least 7 h until the size of particles is reduced as possible. Pellets were prepared from fine grinded powder to analyse the morphology and tribological characteristics by cold pressing, by applying pressure of 8.5 Tonnes/sq.in ($\sim$90 MPa) optimized for 60 s dwell with hydraulic press machine. Figure 3. shows the bar graph between the densities of pure HAp, and its composites filled with $SrCO_3$ and ZrO_2 particles with applied pressure. It shows that the values of densities increases with increasing pressure.

Sample characterizations

The phase formation was characterized by X-ray diffraction method (Rigaku Desktop Miniflex IIX-Ray Diffractometer, Rigaku Corporation,Tokyo Japan) equipped with CuKα radiation and Ni filter. Surface morphologies of the prepared samples were scanned using scanning electron microscopy (Inspect S-50, FEI Company of USA (SEA) PTE Ltd., Singapore, FP 2017/12). A Fourier transform infrared spectrometer (Perkin Elmer spectrum 65, FT-IR spectrometer; Perkin Elmer, MA) was used in the wavenumber range from 4000–400 cm^{-1} to confirm the formation of prepared HAp powder. KBr pellet method was adopted with powder sample in the ratio of KBr:HAp::10:1 by weight. In order to understand the molecular structure of pure HAp, Raman spectroscopy was also done. Raman spectrometer (micro-Raman setup, Renishaw Gloucestershire, UK) equipped with a microscope from Olympus (Model:MX50A/T; Olympus, Hamburg, Germany) was employed. The excitation source was 514.5 nm lines of Ar laser and GRAM-32 (Adept Scientific plc. Hertfordshire,UK) software was used for data collection.

The wear and friction Tribometer is a pin-on-disc type machine (DUCOM model TR-20LE) with facilities to monitor wear and friction in sliding contacts under dry and lubricated conditions that has been used. The elements of the Tribometer is a 'pin' sliding on the flat face of a 'disc' rotating in a vertical plane, with provisions for controlling load, speed and for measuring friction. For our convenience, we measured all the readings in dry conditions. A known load is applied along the axis of the pin and friction force is measured by the force transducer restraining pin motion. Load of the pin
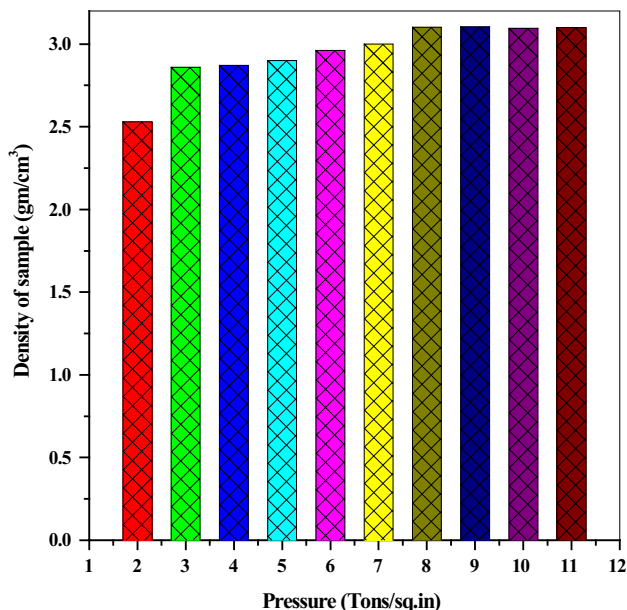
against the disc is applied by placing weights on a pan hanging on a thin steel cable over a pulley and hooked to the arm. Thus the weights pull the pin towards the disc. Tangential frictional force and wear are monitored with electronic sensors and are recorded. The average value of friction coefficient between the stationary pin and the rotating disc with running time (s) and sliding distance (cm) is obtained using wear and friction Tribometer test rig as described above. The principle of operation is that a cantilever loaded pin is sliding against a horizontally rotating cylindrical linear disc. Normal load, rotational speed, wear track length, testing duration and sliding velocity can be varied for suitable testing conditions. All
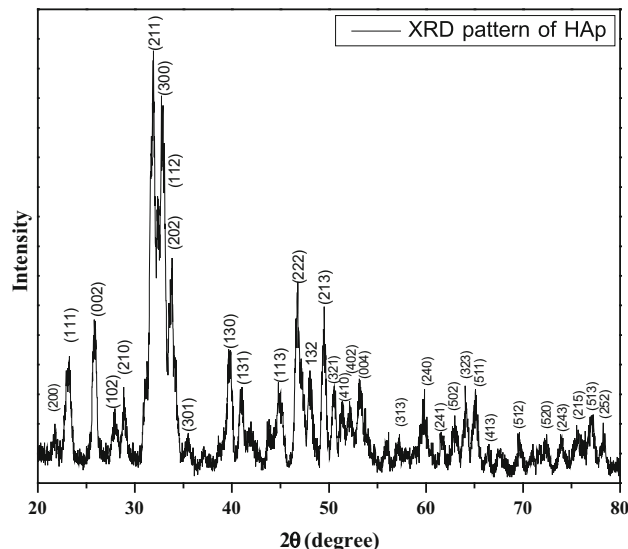

Fig. 4 XRD pattern of nano HAp calcined at 800 °C

Fig. 3 Variation of density with applied pressure for the pure HAp and its composites filled with SrCO₃ and ZrO₂ particles
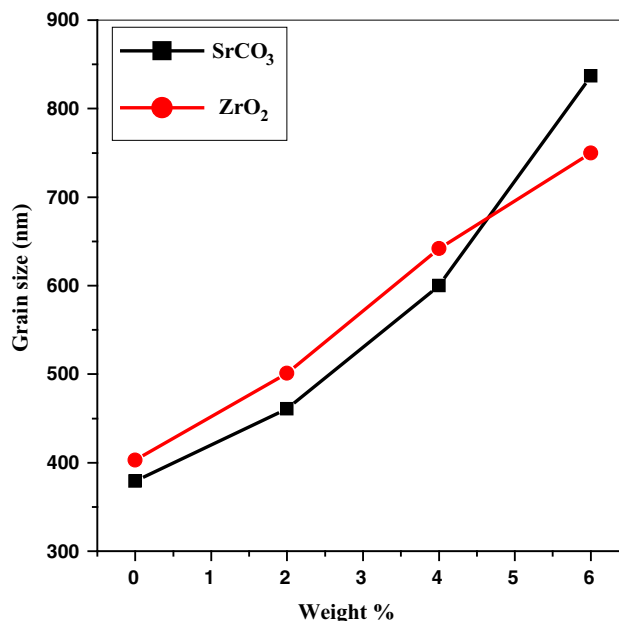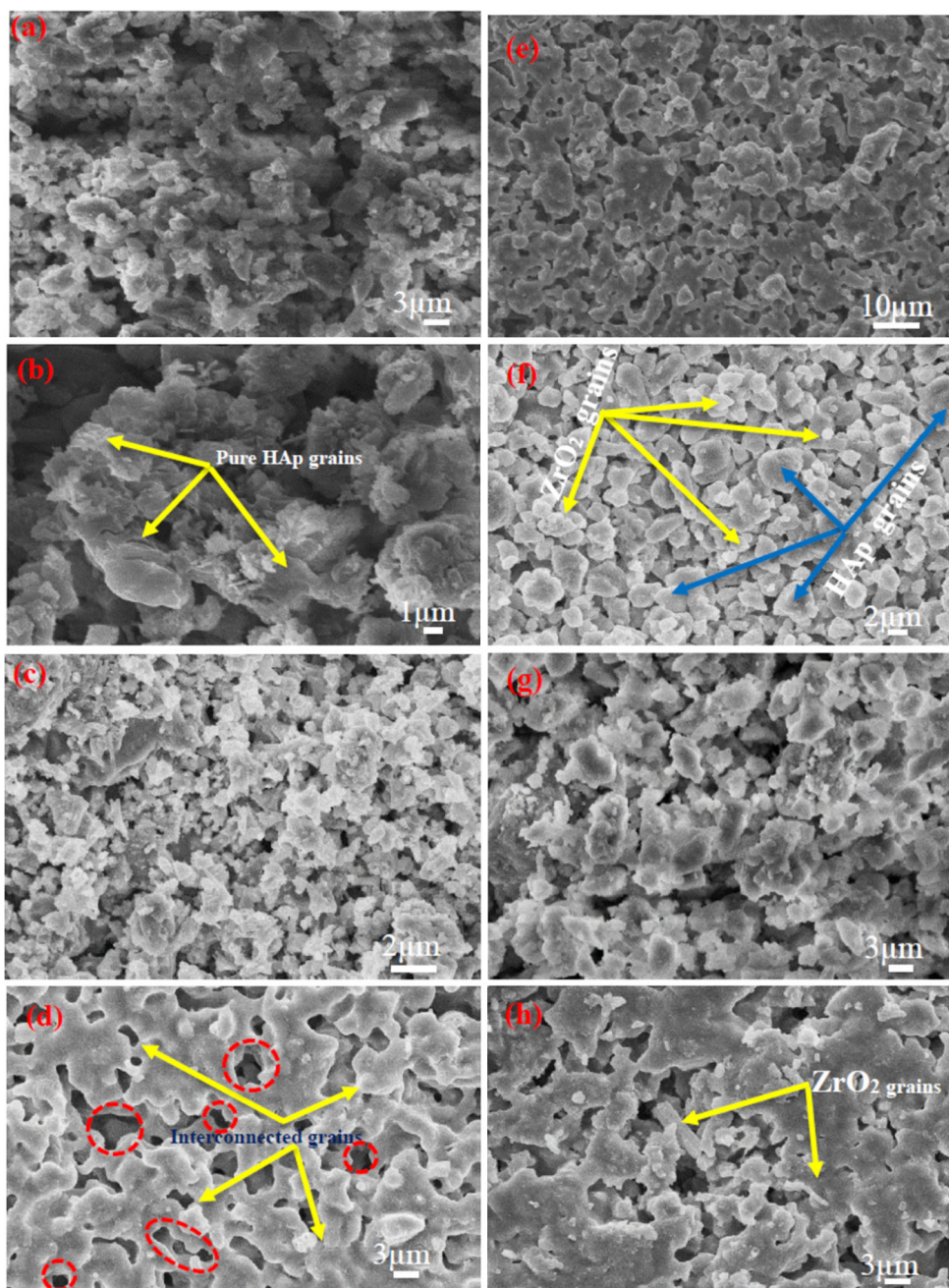

Fig. 5 Variation of grain size versus wt% of SrCO₃ and ZrO₂ (Color figure online)

Fig. 6 SEM micrographs of sintered samples at **a** 1000 °C for HAp, **b** 1100 °C for HAp, **c** 1000 °C for HAp–SrCO$_3$ 2 wt%, **d** 1000 °C for HAp–SrCO$_3$ 4 wt%, **e** 1000 °C for HAp–SrCO$_3$ 6 wt%, **f** 1000 °C for HAp–ZrO$_2$ 4 wt%, **g** 1000 °C for HAp–ZrO$_2$ 4 wt%, **h** 1000 °C for HAp–ZrO$_2$ 6 wt%

the experiments are carried out as per the standard of ASTM G-99.

Results and discussion

X-ray diffraction analysis

The XRD pattern of the HAp powder sample calcined at 800 °C is shown in Fig. 4. XRD pattern has good agreement with the JCPDS (File No. 24-0033) data reported for hexagonal hydroxyapatite. It can be easily seen that most of the peaks of the prepared HAp sample is in coincidence with the standard data of pure HAp. Matching of XRD peaks with JCPDS file concludes the formation of hydroxyapatite via the microwave-assisted synthesis route. The average sizes of the HAp crystallites were estimated using the Scherrer equation (Eq. (2)).

$$D = (0.9\lambda)/(\beta \cos \theta), \tag{2}$$

where D is the average crystallite size of the nanocrystals perpendicular to the crystallographic plane (hkl), λ is the

Table 2 Compositions, sintering temperature, mean grain size, of the sintered samples, peak position of FT-IR spectra along with their assignment for HAp powder calcined at 800 °C

Compositions	Sintering temp. (°C)	Grain size (nm)	Wavelength of different absorption peaks (cm^{-1}) of HAp calcined at 800 °C	Assignment
HAp	1000	379	477	υ_2 stretching mode of PO_4^{3-}
HAp	1100	403	540	υ_4 bending mode of O–P–O
HAp–SrCO$_3$ 2 wt%	1000	461	646	Liberation mode of OH$^-$ band
HAp–SrCO$_3$ 4 wt%	1000	600	1458	υ_3 carbonate ion of (CO_3^{2-})
HAp–SrCO$_3$ 6 wt%	1000	837	1636	υ_3 carbonate ion of (CO_3^{2-})
HAp–ZrO$_2$ 2 wt%	1000	501	1984	P–O asymmetric stretching
HAp–ZrO$_2$ 4 wt%	1000	642	2219	P–O asymmetric stretching
HAp–ZrO$_2$ 6 wt%	1000	750	3572	stretching mode of OH$^-$ band
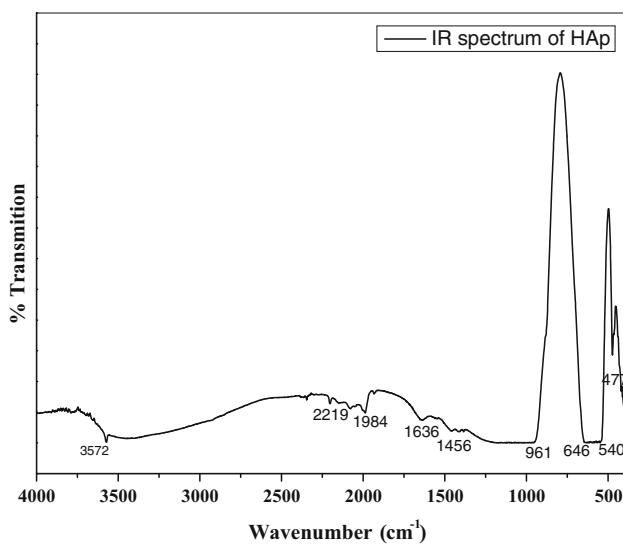
Fig. 7 FT-IR spectroscopy of HAp calcined at 1000 °C
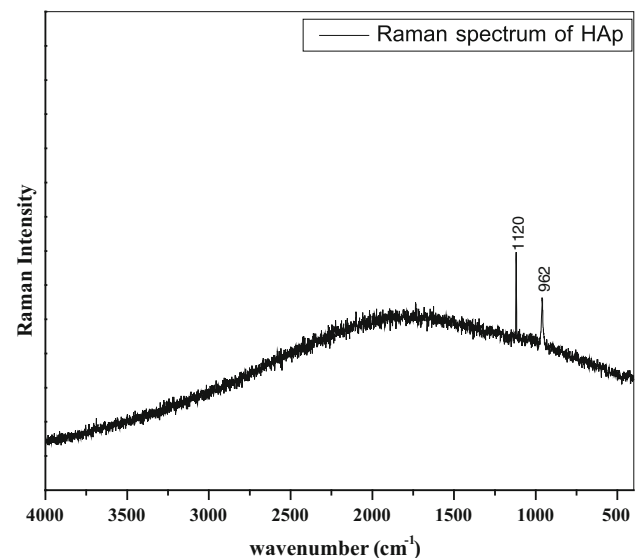
Fig. 8 Raman spectroscopy of HAp

X-ray wavelength of diffractometer CuKα (0.15406 nm), β is the full width at half maximum (FWHM) intensity in radians and θ is the diffraction peak angle. The average crystalline sizes of the samples estimated are displayed in Fig. 5. The variation of grain size versus weight percentage of the SrCO$_3$ and ZrO$_2$ samples are shown in Fig. 5. It is clear that, by increasing wt% concentration of SrCO$_3$ and ZrO$_2$, the average grain size is increases. This is due to the nucleation and growth of the grains during the sintering process. This essentially leads to the conclusion that average crystallite size of calcined powder sample comes out to be 30 ± 5 nm. The X-ray phase analysis revealed that all major as well as minor peaks of HAp are present in the XRD pattern of prepared HAp powder. The energy given by the microwave radiation was sufficient to evolve major high intensity peaks of HAp corresponding to

various planes viz., (111), (002), (211), (112), (300), (202), (301) and (310), respectively.

The surface morphological analysis of the samples

To study the morphology of HAp powder as well as their composite ceramics, SEM has been carried out. The SEM images of pure HAp sintered at 1000 and 1100 °C are shown in Fig. 6a–b at the resolution of 3 and 1 μm, respectively. Figure 6c–e shows the microstructures of composites of HAp with varying (c) 2, (d) 4 and (e) 6 wt% of SrCO$_3$ calcined at 1000 °C and at the resolution of 2, 3 and 10 μm, respectively. However, the microstructures of HAp composite with varying (f) 2, (g) 4 and (h) 6 wt% of ZrO$_2$ calcined at 1000 °C and at resolution of 2, 3 and 3 μm, respectively are shown in Fig. 6f–h. The mean grain

sizes of the prepared HAp and its composite samples are enlisted in Table 2. The calculations for grain size analysis were also carried out using SEM images. The mean particle sizes of the HAp composite with 2, 4 and 6 wt% of $SrCO_3$ content were found to be $\sim$461, 600 and 750 nm, respectively. It can be seen that the samples are tiny distorted spheres which are attached together and form agglomerated 3-D structure and enhanced the strength of the material. This may be due to diffusion of ceramic particles at high temperature. Whereas, the mean particle sizes of the samples with 2, 4 and 6 wt% of ZrO_2 content were estimated to be 501, 642 and 837 nm, respectively. Particles size of HAp composites having ZrO_2 content is larger than the $SrCO_3$-contained HAp composites for each wt%. This reveals that the presence of ZrO_2 among HAp NP particles promotes the grain growth comparatively more than that of $SrCO_3$ during the sintering.

From Fig. 6c–h it is clear that as the doping wt% increases and there is a slow transformation that occurs from coarse to fine grain size might be due to the neck formation. The SEM images of composites (Fig. 6d, e) show a porous bulk network between the HAp and the $SrCO_3$ grains. On the other hand, SEM micrographs of HAp composite with ZrO_2 (Fig. 6f, h) showed fully developed and randomly oriented grains of HAp and ZrO_2. The grain sizes were proportional to the weight percentage of the $SrCO_3$ and ZrO_2.

FT-IR and Raman spectroscopic analysis

Fourier transform infrared spectrum of HAp powder sintered at 1000 °C is shown in Fig. 7. The observed bands along with their assignment are enlisted in Table 2. Most of the observed bands are attributed to one or other vibrational modes of different functional groups present in pure HAp. The sharp shoulder at 3572 cm^{-1} is due to the symmetric stretching mode of OH^- of water [25, 26]. A broad envelope centered around 3443 cm^{-1} is assigned to O–H stretching. However, its (H–O–H) bending mode is observed at 1636 cm^{-1}. The band appeared at 1458 cm^{-1} and is attributed to CO_3^{2-} which might be a substitute to PO_4^{3-} during synthesis. A shoulder recorded at 961 cm^{-1} is assigned to ν_1 symmetric stretching of P–O of phosphate (PO_4^{3-}) group. The vibration of OH^- is observed at 646 cm^{-1}. A shoulder observed at 540 cm^{-1} is attributed to the ν_4 asymmetric bending mode of O–P–O in PO_4^{3-} group. A band at 477 cm^{-1} is also observed due to ν_2 symmetric bending mode of O–P–O in PO_4^{3-} group. The IR absorption bands at 2219 and 1984 cm^{-1} spectrum could not be attributed to any specific vibration of HAp. These absorption bands may be due to the impurities. Raman spectrum of HAp powder sample calcined at 800 °C is shown in Fig. 8. Raman pattern exhibits only a

couple of sharp peaks located at 1120 and 962 cm^{-1} which appears due to ν_3 asymmetric and ν_1 symmetric stretching modes of P–O in PO_4^{3-}, respectively.

Tribological analysis

The size of the grains of the samples and thermal properties influence the wear characteristics, as the grain size of ceramic is an important parameter to improve the wear characteristics in dry sliding. Hand grinding techniques
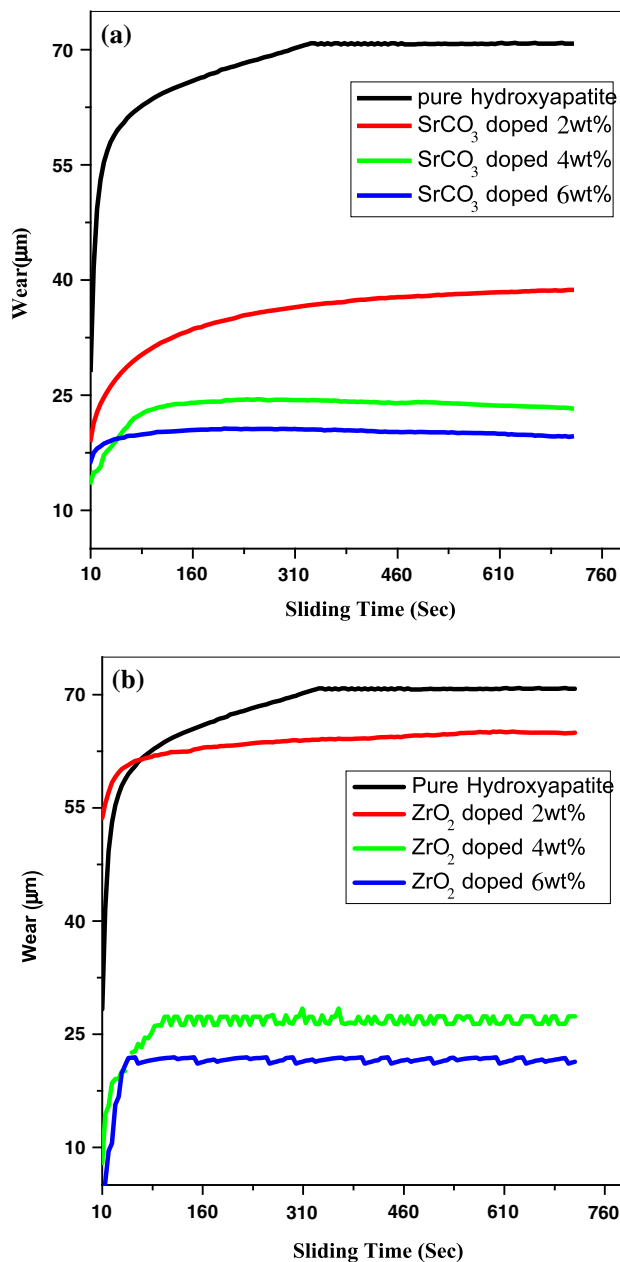

Fig. 9 Variation of wear against sliding time at load 300 N with sliding velocity of 3 m/s for a HAp and HAp–$SrCO_3$ of different wt% b HAp and HAp–ZrO_2 of different wt% (Color figure online)

Table 3 Compositions, sintering temperature, density, mass loss, volume loss and specific wear rates tested at 30 N

Compositions	Sintering temp. (°C)	Density (gm/cm³)	Mass loss (Δm) during sliding (gm)	Volume loss (ΔV) mm³	Specific wear rate (Ws) in mm³/Nm
HAp	1000	3.1483	0.0106	3.366896	6.3557×10^{-5}
HAp	1100	3.1530	0.0153	4.852521	9.16019×10^{-5}
HAp	1200	3.1240	0.1061	33.96287	6.41123×10^{-4}
SrCO₃ doped 2 wt%	1000	3.2241	0.0093	2.884526	5.44517×10^{-5}
SrCO₃ doped 4 wt%	1000	3.3001	0.0085	2.57568	4.86216×10^{-5}
SrCO₃ doped 6 wt%	1000	3.3804	0.0074	2.18909	4.13239×10^{-5}
ZrO₂ doped 2 wt%	1000	3.1560	0.0102	3.231939	6.10099×10^{-5}
ZrO₂ doped 4 wt%	1000	3.2685	0.0091	2.784152	5.25569×10^{-5}
ZrO₂ doped 6 wt%	1000	3.3832	0.0084	2.482856	4.68693×10^{-5}

have been used to reduce the particle size from micrometres to nanometre which helps the grains to attach and form agglomerates (Table 2). The mean grain size and bonding strength among the composition enhance with doping of SrCO₃ in pure HAp which results in the decrease of wear as illustrated in Fig. 9a, whereas the mean grain size of the samples with ZrO₂ content in 2, 4 and 6 wt% were approximately 501, 642 and 750 nm, respectively. Similarly with the decrease in grain size of hydroxyapatite doped with ZrO₂ the wear decreases as illustrated in Fig. 9b. The average grain size of HAp–ZrO₂ is greater than that of the average grain size of HAp–SrCO₃, this may lead to higher wear of hydroxyapatite-doped ZrO₂ as compared to hydroxyapatite-doped SrCO₃. As the mean grain size decreases the grains attached together and form agglomerates, thus leading to form high bonding between HAp molecules and dopants, which acts as reinforcement. The specific wear rate and wear of HAp-doped SrCO₃ decreases from 5.44517×10^{-5} to 4.13239×10^{-5} mm³/ Nm. Similarly HAp doped for ZrO₂ from 6.10099×10^{-5} to 4.68693×10^{-5} mm³/Nm, respectively and is listed in Table 3.

$$Ws = \frac{(\Delta V)1000}{LP} = \frac{((m1 - m2)/\rho)1000}{LP}, \tag{3}$$

where ΔV is the volume loss (mm³), ρ is the density of sample (gm/cm³), P is the applied load (N), L is the sliding distance (m), $m1$ is the weight before test (N) and $m2$ is the weight after test (N).

From Fig. 10a and b, it is seen that, in case of pure hydroxyapatite the specific wear rate (Ws) increases with increase in sintering temperature and have high wear and high specific wear rate as compared to HAp-doped SrCO₃ and ZrO₂. This trend may be due to high sintering temperature that exceeds the crystallization temperature. Whereas, in case of pure hydroxyapatite, as there is no any
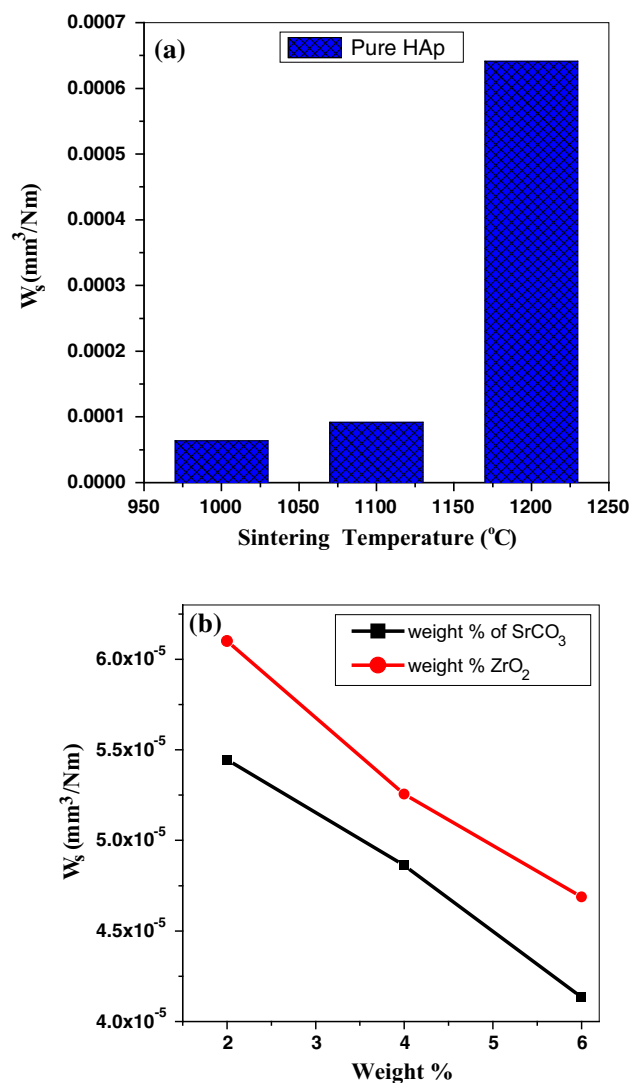

Fig. 10 Variation of specific wear rates **a** pure HAp against sintering temperature **b** HAp–SrCO₃ and HAp–ZrO₂ against wt% (Color figure online)

Fig. 11 Variation of
a frictional force against sliding
time for HAp–SrCO₃,
b coefficient of friction against
sliding time for HAp–SrCO₃,
c frictional force against sliding
time for HAp–ZrO₂,
d coefficient of friction against
sliding time for HAp–ZrO₂, **e** all
sample coefficient of friction
against wt% (Color
figure online)
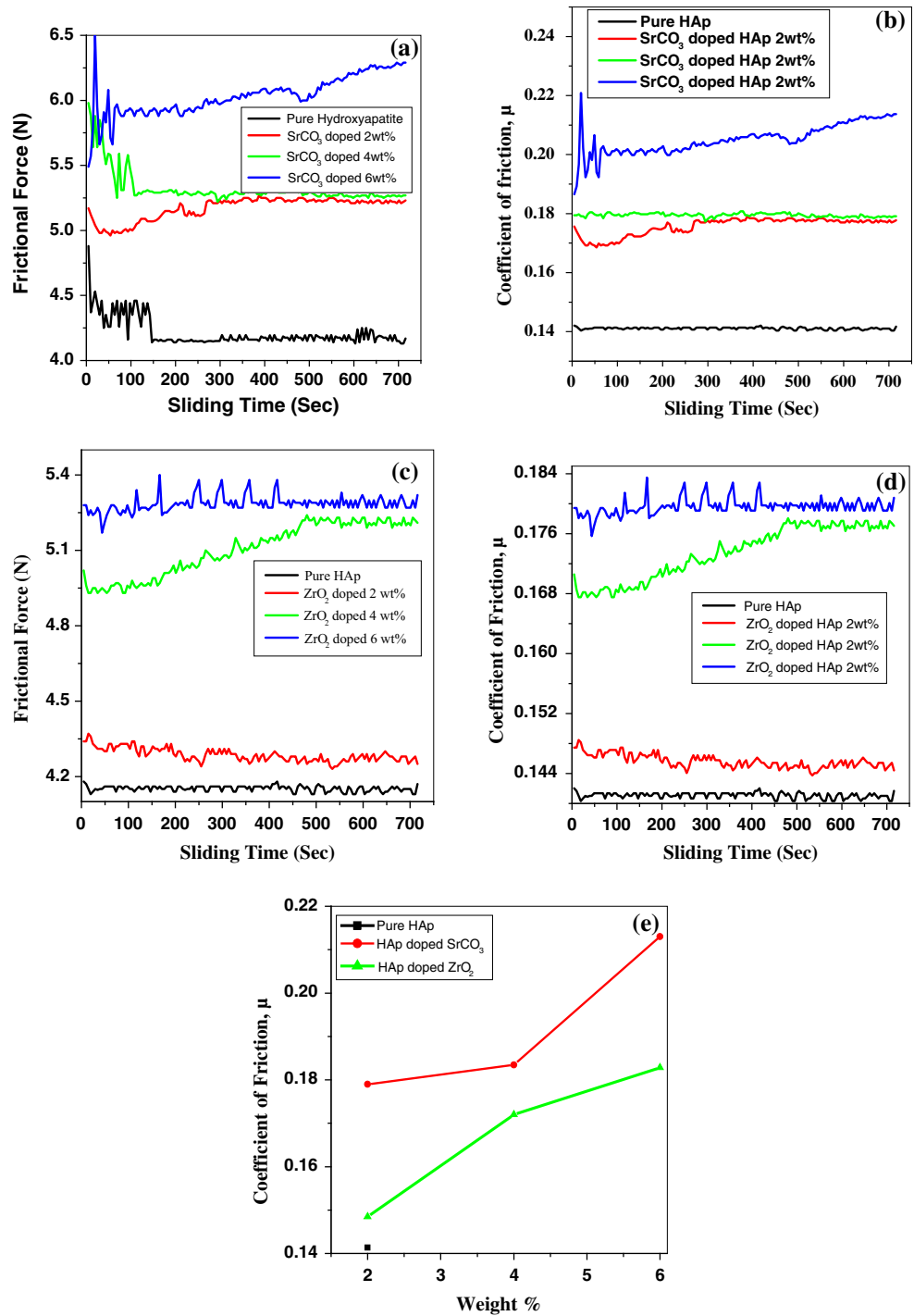
reinforcement bonding between the molecules as compared to the doped HAp and it results in the removal of debris from larger patches and starts wear process in pure HAp. Also asperities on rotating steel disc exhibits plugging action on the weak bonding surface of the HAp and cause higher specific wear rate approximately of the order of 6.3557×10^{-5} mm³/Nm.

The graphs for friction force and coefficient of friction of pure HAp and HAp–SrCO₃ of various wt% plotted against sliding time are shown in Fig. 11a and b. As we see that the friction value initially increases during running-in period but became steady after sliding some distance for all wt%. It is believed that within the running-in period, the ridges are formed on the surface of the ceramic but during

the steady-state period, these ridges disappear and wear debris covers the surface, which lead to lower friction coefficient and frictional force values [31]. Since the composite ceramic is brought to sliding contact with metal disc, strong adhesion force occurs which results in high friction and transfer of material between the sample and metal disc. As the material transfer increases along with increase in $SrCO_3$, the tribo-system change from ceramic–metal contact to metal–metal contact tribo-system [32], these would be the reason for coefficient of friction to increase from 0.17901 to 0.2130 with the increase in wt% of doping. Coefficient of friction of zirconium increases with increase in the value of sliding temperature and time [33]. The plots of friction force and coefficient of friction for HAp–ZrO_2 are plotted in Fig. 11c and d, respectively. It is seen that varying the wt% of HAp–ZrO_2 the friction force as well as friction coefficient of samples increases simultaneously with increase in ZrO_2 concentration. The coefficient of friction tends to vary in between 0.14 and 0.185. However, the trends of the both the results are similar in nature. In the present study, applied normal load of 30 N with variation in wt% of ZrO_2 has been considered. It was observed that ceramics like ZrO_2, Al_2O_3 forms oxide layer at high sliding temperature and succeed in lowering the friction from 0.4 to 0.14 under various loads ranging from 18 to 80 N [33]. This can be the reason for lowering in coefficient of friction of ZrO_2 as compared to $SrCO_3$ of corresponding wt% as shown in Fig. 11e. The composite with ZrO_2 has higher wear and lower friction for all the contents than the ones with $SrCO_3$. The another possible reason is that the higher wear of the composites with ZrO_2 lowers the interfacial shear strength between rubbing surfaces via the higher surface roughening of rubbing surfaces and the larger amount of wear debris and gives rise to their lower friction since an effective interfacial shear strength between two contacting surfaces results in a high friction.

Conclusions

In the reported work, single phase of HAp (with crystallite size of 30 ± 5) using microwave irradiation technique and its composites with 2, 4 and 6 wt% $SrCO_3$ and ZrO_2 individually have been successfully synthesized. Simultaneous characterizations by XRD, IR and Raman techniques not only convince but confirm the formation of HAp via microwave-assisted synthesis route. Microstructural investigations of these composite bioceramic reveal that the $SrCO_3$ and ZrO_2 affect the grain growth during heat treatment. However, the effect of ZrO_2 on grain size is more than the $SrCO_3$, as the ZrO_2 contained composites have larger grain sizes. Accordingly the tribological characteristics of HAp and its different composites with 2, 4 and 6 wt% $SrCO_3$ and ZrO_2 were also studied with sliding velocity of 3 cm/s under the load of 30 N. The tribological investigations of HAp and its composites revealed that inclusion of $SrCO_3$ and ZrO_2 in pure HAp significantly enhanced the resistance to wear and specific wear rate. Increase in wt% of additives gives rise to the better wear resistance and specific wear rate. Due to the high wear resistance of this HAp–ZrO_2 composite material, it can be used as bioceramic materials.

References

1. Hench LL, Wilson J (1984) Surface-active biomaterials. Science 226:630–636
2. Hench LL, Splinter RJ, Allen WC, Greenlee TK (1971) Bonding mechanisms at the interface of ceramic prosthetic materials. Biomed Mater Res 5:117–141
3. Roy M, Bandyopadhyay A, Bose S (2011) Induction plasma sprayed Sr and Mg doped nano hydroxyapatite coatings on Ti for bone implant. J Biomed Mater Res 99B:258–265
4. Santavirta S, Takagi M, Nordsletten L, Anttila A, Lappalainen R, Konttinen YT (1998) Biocompatibility of silicon carbide in colony formation test in vitro A promising new ceramic THR implant coating material Clinical and Exp. Forum 118:89–91
5. Hench LL, Polak JM, Xynos ID, Buttery LDK (2000) Bioactive materials to control cell cycle. Mater Res Innov 3:313–323
6. Dorozhkin SV (2010) Calcium orthophosphates as bioceramics: state of the art. J Funct Biomater 1:22–107
7. Yazdanpanah Z, Bahrololoom ME, Hashemi B (2015) Evaluating morphology and mechanical properties of glass-reinforced natural hydroxyapatite composites. J Mech Behav Biomed Mater 21:36–42
8. Hench LL (1991) Bioceramics: from concept to clinic. J Am Ceram Soc 74:1487–1510
9. Mobasherpour I, Heshajin MS, Kazemzadeh A, Zakeri M (2007) Synthesis of nanocrystalline hydroxyapatite by using precipitation method. J Alloys Compd 430:330–333
10. Regi MV, Colilla M, Gonzalez B (2011) Medical applications of organic-inorganic hybrid materials within the field of silica-based bioceramics. Chem Soc Rev 40:596–607
11. Yuhta T, Kikuta Y, Mitamura Y, Nakagane K, Murabayashi S, Nishimura I (1994) Direct bone formation on alumina bead composite. J Biomed Mater Res 28:217–224
12. Zeng S, Cao W, Liu G (1995) Biological evaluation of bioceramic materials-a review. Int Symp Ceram Med 8:461–464
13. Nathanael AJ, Mangalaraj D, Chen PC, Ponpandian N (2011) Enhanced mechanical strength of hydroxyapatite nanorods reinforced with polyethylene. J Nanopart Res 13:1841–1853
14. Asgharzadeh H, Shirazi MR Ayatollahi, Naimi-Jamal MR (2015) Influence of hydroxyapatite nano-particles on the mechanical and tribological properties of orthopedic cement-based nano-

composites measured by nano-indentation and nano-scratch experiments. J Mater Eng Perform 24:3300

15. Lahiri D, Singh V, Benaduce AP, Sealb S, Kos Lidia, Agarwal A (2011) Boron nitride nano tube reinforced hydroxyapatite composite: mechanical and tribological performances and in-vitro-biocompatibility to osteoblasts. J Mech Behav Biomed Mater 4:44–56

16. Ayatollahi MR, Yahya MY, Shirazi HA, Hassan SA (2015) Mechanical and tribological properties of hydroxyapatite nanoparticles extracted from natural bovine and the bone cement developed by nano- sized bovine hydroxyapatite filler. Ceram Int 41:10818–10827

17. Bodhak S, Nath S, Basu B (2009) Friction and wear properties of novel HDPE-HAp-Al₂O₃ biocomposites against alumina counterface. J Biomater Appl March 23:407–433

18. Zhou C, Deng C, Chen X, Zhao X, Chen Y, Fan Y, Zhang X (2015) J Mech Behav Biomed Mater 48: 1–11

19. André RS, Paris EC, Gurgel MFC, Rosa ILV, Paiva-Santos CO, Li MS, Varela JA, Longo E (2012) Structural evolution of Eu-doped hydroxyapatite nanorods monitored by photoluminescence emission. J Alloys Compd 531:50–54

20. Menea RU, Mahabole MP, Mohite KC, Khairnar RS (2014) Fe doped hydroxyapatite thick films modified via swift heavy ion irradiation for CO and CO₂ gas sensing application. J Alloys Compd 584:487–493

21. Mishra VK, Bhattacharjee BN, Parkash O, Kumar D, Rai SB (2014) Mg-doped hydroxyapatite nanoplates for biomedical applications: a surfactant assisted microwave synthesis and spectroscopic investigations. J Alloys Compd 614:283–288

22. Shih WJ, Chen YF, Wang MC, Hon MH (2004) Crystal growth and morphology of the nano- sized hydroxyapatite powders synthesized from CaHPO₄·2H₂O and CaCO₃ by hydrolysis method. J Cryst Growth Des 270:211–218

23. Fathi MH, Hanifi A (2007) Evaluation and characterization of nanostructure hydroxyapatite powder prepared by simple sol gel method. Mater Lett 16:3978–3983

24. Yoshimura M, Suda H (1994) Effect of operation conditions on HA synthesized by the hydrothermal method. J Mater Sci 29:51–54

25. Mishra VK, Srivastava SK, Asthana BP, Kumar D (2012) Structural and spectroscopic studies of hydroxyapatite nanorods formed via microwave-assisted synthesis route. J Am Ceram Soc 95:2709–2715

26. Mishra VK, Rai SB, Asthana BP, Parkash O, Kumar D (2014) Effect of annealing on nanoparticles of hydroxyapatite synthesized via microwave irradiation: structural and spectroscopic studies. Ceram Int 40:11319–11328

27. Liu J, Li K, Wang H, Zhu M, Xu H (2005) Self-assembly of hydroxyapatite nanostructures by microwave irradiation. Nanotechnology 16:82–87

28. Qian WY, Sun DM, Zhu RR, Du XL, Liu H, Wang SL (2012) pH-sensitive strontium carbonate nanoparticles as new anticancer vehicles for controlled etoposide release. Int J Nanomed 7:5781–5792

29. Sennerby L, Dasmah A, Larsson B, Iverhed M (2005) Bone tissue responses to surface- modified zirconia implants: a histomorphometric and removal torque study in the rabbit. Clin Implant Dent Relat Res 7:S13–S20

30. Brüll F, Winkelhoff AJ, Cune MS (2014) Zirconia dental implants: a clinical, radiographic and microbiologic evaluation up to 3 years. Int J Oral Maxillofac Implant 29(4):914–920

31. Quinn TFJ (1983) Review of oxidational wear, part I: the origins of oxidational wear. Tribol Int 16:257–271

32. Xu J, Kato K (2000) Formation of tribochemical layer of ceramics sliding in water and its role for low friction. Wear 247:61–75

33. Sasaki S (1992) Bull Mech Eng Lab 134:67–89